Advances in Differential Equations and Control Processes 2026, 33(2), 4172.
doi: https://doi.org/10.59400/adecp4172

Article

A numerical approach to magnetic field calculation in Hall thrusters considering nonlinear magnetic permeability with Aitken extrapolation for convergence acceleration

Jiasong Li, Yanbin Xi, Yue Liu*

School of Physics, Dalian University of Technology, Dalian 116024, China

*** Corresponding author:** Yue Liu, liuyue@dlut.edu.cn

CITATION

Li J, Xi Y, Liu Y. A numerical approach to magnetic field calculation in Hall thrusters considering nonlinear magnetic permeability with Aitken extrapolation for convergence acceleration. Advances in Differential Equations and Control Processes. 2026; 33(2): 4172. https://doi.org/10.59400/adecp4172

ARTICLE INFO

Received: 18 March 2026
Revised: 10 May 2026
Accepted: 17 May 2026
Available online: 3 June 2026

Abstract: This paper investigates the numerical computation of magnetic fields in a Hall thruster, a process governed by a nonlinear elliptic boundary value problem. The model rigorously accounts for the influence of ferromagnetic materials, where the relative permeability is defined as a magnetic field-dependent function exceeding unity in core regions and set to unity elsewhere. Consequently, the model equations are inherently nonlinear, and their coefficients exhibit discontinuity across material interfaces. To solve this complex system, the finite difference method is applied on a uniform staggered mesh to derive a system of nonlinear difference equations with discontinuous coefficients. An iterative algorithm featuring a nested loop structure is presented to tackle this nonlinearity: an inner loop computes the magnetic field for a fixed relative permeability, while an outer loop updates the permeability distribution based on the current field solution. A critical challenge in such simulations is the convergence difficulty under high excitation due to strong nonlinearity and magnetic saturation. To address this, we propose a robust nested iterative algorithm enhanced with Aitken extrapolation. The method is validated through numerical simulations on a miniature Hall thruster model across three distinct coil ampere-turn configurations. Results highlight a critical distinction: while the standard fixed-point iteration performs adequately under low-to-moderate excitation, it fails to converge under the high-excitation condition. In contrast, the proposed Aitken-accelerated algorithm achieves stable convergence across all test cases, successfully resolving the convergence bottleneck in high-field scenarios. This advancement provides a robust framework for the magnetic circuit design of high-power Hall thrusters.

Keywords: Hall thruster; magnetic field calculation; nonlinear magnetic permeability; finite difference method; nested iteration; Aitken extrapolation; convergence acceleration; magnetic circuit design

1. Introduction

A new era of space exploration is dawning, driven by ambitious deep-space missions and intensifying competition among governments to expand humanity's reach. As the scope of space utilization grows ever deeper, conventional chemical propulsion can no longer meet the demands of future exploration—particularly for deep-space travel and low-Earth orbit control [1,2]. Consequently, nations worldwide are actively investigating a variety of cutting-edge propulsion technologies, with electric propulsion emerging as a primary focus of current development.

Hall thrusters stand as a highly effective electric propulsion technology, proving

indispensable for modern aerospace applications. By accelerating ionized propellant through the synergistic interaction of electric and magnetic fields, these devices generate thrust [3]. They outperform conventional chemical propulsion systems by achieving higher exhaust velocities, which translates to superior specific impulse and thrust-to-power ratios [4]. This capability enables extended periods of continuous thrust while drastically reducing propellant mass. Consequently, Hall thrusters are ideally suited for interplanetary transfers, deep-space exploration, interstellar missions, and for precise attitude control and orbital maneuvers on both geostationary and low Earth orbit satellites [5].

The rapid expansion of low-Earth orbit satellite constellations and the global shift toward electric propulsion have placed increasingly stringent demands on Hall thrusters, particularly regarding miniaturization, power efficiency, and operational lifespan [6]. The configuration and strength of the background magnetic field are critical determinants of the thruster's performance, discharge characteristics, and longevity, making it a cornerstone of the operating principle [7]. Consequently, optimizing thruster design and enhancing performance require a detailed understanding of, and precise control over, the background magnetic field.

The Hall thruster features an annular channel where electromagnetic coils or permanent magnets generate a radial magnetic field [8]. Simultaneously, an axial electric field is established by applying a potential difference between the anode and cathode positioned externally [9]. Due to the perpendicular orientation of these electric and magnetic fields ($\boldsymbol{E} \times \boldsymbol{B}$), electrons within the channel exhibit rapid azimuthal motion—perpendicular to both field vectors—generating a drift current known as the Hall current [10]. This Hall drift significantly suppresses the axial electron flow from cathode to anode, thereby enhancing ionization efficiency. Given their significantly higher mass, ions are less susceptible to magnetic field influence under optimal conditions. Consequently, the axial electric field accelerates these newly formed positive ions, expelling them at high velocity to generate thrust [11].

The development of Hall thrusters traces back to the late 1950s when Soviet scientists first introduced the concept of Hall-effect electric propulsion [12]. Askold Zharinov pioneered the Anode Layer Thruster (TAL), laying the groundwork for future innovations [13]. This was followed in 1962 by Alexey Morozov's proposal of the Stationary Plasma Thruster (SPT), which quickly gained traction [14]. Throughout the 1960s, the SPT design made significant strides, ultimately emerging as the dominant pathway for Hall-effect electric propulsion technology.

The design and optimization of the background magnetic field remain a critical focus in Hall thruster research, as configuration directly influences key performance metrics—including thrust, specific impulse, and efficiency. To achieve greater flexibility in generating and regulating these fields, researchers have explored various methodologies. Historically, electromagnetic coils served as the primary means of field generation. However, due to their independence from external power sources, permanent magnets have gained prominence in low-power applications, particularly for microsatellites, offering a distinct advantage in reducing overall propulsion power requirements [15]. The latest frontier in this domain is hybrid field generation

technology. By combining permanent magnets and electromagnetic coils, this approach leverages the efficiency of permanent magnets for establishing the primary field, while utilizing coils to fine-tune the field for enhanced adaptability [16]. This synergy extends the operational range and further elevates thruster performance.

In the early days of Hall thruster development, when computational resources were limited, magnetic field design relied primarily on simplified analytical techniques and empirical experimentation. Under axisymmetric assumptions, analytical methods utilized Maxwell's equations to formulate mathematical models, which were then discretized via finite difference methods and solved numerically using iterative algorithms [17, 18]. Concurrently, experimental research involved varying the current in magnetic coils to investigate diverse configurations and their impact on performance. For instance, studies on cylindrical Hall thrusters examined common coil configurations—specifically co-current and counter-current setups—and their effects on ion beam characteristics. Results indicated that the co-current configuration enhances propellant efficiency and ion current [7]. This demonstrates that modulating the magnetic field's strength and topology directly influences ionization and acceleration processes, thereby optimizing thruster performance. Additionally, magnetic focusing techniques have been employed in low-power thrusters to mitigate large plume divergence angles [19]. Modern design and optimization must also account for various complex factors, including the impact of asymmetric magnetic fields on discharge behavior in high-aspect-ratio channels and the influence of magnetic field peak positioning on discharge characteristics [20,21].

The rapid advancement of computer technology has led to the widespread adoption of numerical simulation techniques in Hall thruster magnetic field calculations. Among these, the Finite Element Method (FEM) is a prevalent technique capable of accurately simulating complex magnetic field distributions [22]. Using FEM software such as Maxwell, researchers systematically investigate how variables—including coil geometry and current magnitude—influence magnetic field topology [23, 24]. To simulate plasma-magnetic field interactions and gain a more comprehensive understanding of operational mechanisms, Particle-in-Cell (PIC) and fluid dynamics models are extensively employed. Notably, studies demonstrate that the PIC-MCC method can effectively simulate the impact of magnetic field gradients on the performance of magnetically shielded Hall thrusters [25, 26]. These numerical simulations not only facilitate in-depth analysis of internal physical processes that are experimentally inaccessible but also significantly reduce experimental costs.

To achieve a more precise representation of multiphysics field coupling, researchers have developed integrated fluid simulation platforms. For instance, the DUT-HTFS platform utilizes three distinct meshes dedicated to geometric, magnetic field, and plasma calculations, respectively, thereby integrating these modules [27,28]. Application of this platform has further elucidated the impact of magnetic fields on plasma characteristics, revealing a significant influence on plasma density distribution—particularly in the radial direction within the ionization region and near the anode. This underscores the critical dependence of plasma confinement and acceleration processes on the magnetic field configuration.

The most significant advancement in Hall propulsion technology in recent years is the development of magnetically shielded Hall thrusters [29,30]. Traditional designs face a critical limitation: wall erosion caused by ion bombardment severely restricts their operational lifespan. Magnetic shielding overcomes this challenge by optimizing the magnetic field topology to create a ”magnetic barrier” [31]. By bending the magnetic field lines at the channel exit, this barrier deflects high-energy ions away from the walls, drastically extending the thruster's longevity. For instance, rear-field technology prolongs the operational life by modifying the magnetic field distribution, thereby shifting the ionization and acceleration zones downstream and effectively suppressing wall bombardment [32].

The efficacy of magnetic shielding is highly contingent upon the precise magnetic field configuration, making magnetic circuit optimization a critical aspect of Hall thruster design [33, 34]. The primary objective is to generate an annular magnetic field distribution characterized by a high gradient, high uniformity, and minimal magnetic leakage, thereby aligning with the optimal ionization zone and electron confinement requirements [35]. This optimization is achieved by finely controlling the field distribution through the adjustment of excitation coil parameters—including current, number of turns, geometry, and spatial positioning. Furthermore, the geometry of the magnetic poles, particularly the chamfer design [36], along with their dimensions and relative positioning, plays a pivotal role in shaping magnetic flux lines and field intensity to ensure optimal shielding performance.

Magnetic circuit optimization typically integrates numerical simulation with parametric optimization algorithms. Initially, Finite Element Method software is employed to simulate the magnetic field, allowing researchers to predict and evaluate the field distribution of various magnetic circuit configurations prior to fabrication [37]. Building on this, local or global optimization algorithms are applied to conduct multi-objective optimization. This approach aims to achieve an effective balance among key performance metrics, including thrust, efficiency, lifetime, and plume divergence [38–41].

In summary, the magnetic shielding technology of Hall thrusters significantly extends the device's operational lifetime by mitigating channel wall erosion through optimized magnetic field configurations. As the core enabler of this technology, magnetic circuit optimization involves the refined design of excitation parameters and geometric structures. Therefore, the optimization of the magnetic field in Hall thrusters is not only critical for achieving efficient magnetic shielding but also constitutes the central focus of this study.

Most commercial software currently employed to compute Hall thruster magnetic fields relies on the assumption of fixed relative permeability for ferromagnetic materials to simplify calculations. However, the relative permeability of these materials is inherently nonlinear with respect to the magnetic field. While iterative techniques are utilized to solve the elliptic partial differential equations governing magnetic field profiles, these traditional approaches lack a theoretical proof of convergence and may diverge, particularly under conditions of high excitation. To address these critical limitations, this study aims to develop an accurate, robust, and self-contained numerical

method for nonlinear magnetic field calculation. The main contributions and novelties of this work are summarized as follows:

(1) A fully consistent axisymmetric FDM model with a nonlinear $\mu(B)$ relation.

(2) A nested iterative scheme for magnetic vector potential and permeability.

(3) Introduction of Aitken extrapolation to stabilize convergence under high excitation.

This paper is structured as follows: A model for the magnetic field of a Hall thruster is established in Section 2. Section 3 introduces two iterative algorithms for computing the Hall thruster magnetic field. In Section 4, three numerical examples are provided, along with an analysis and discussion of the results. Finally, a summary concludes the paper.

2. Model

Consider a cylindrical Hall thruster encased in ceramic, featuring a toroidal straight channel. A cathode is connected to the outer end of the channel to emit electrons, while an anode with a gas inlet is connected to the inner end. These two electrodes establish an axial electric field with the plasma generated by ionized propellant gas within the channel. There are several coils in the wall of the thruster. The coils generate a radial magnetic field inside the channel. Under the combined influence of the axial electric field and radial magnetic field, magnetized electrons are effectively confined within the channel, forming a Hall current that significantly enhances the ionization efficiency. Concurrently, unmagnetized ions are accelerated and ejected by the axial electric field to generate thrust. To optimize plasma confinement and ion acceleration, the ferromagnetic material is incorporated into the thruster to manipulate the magnetic flux path, thereby enabling the precise construction of the required magnetic field gradient and topology. A schematic diagram of the Hall thruster cross-section is shown in **Figure 1**.

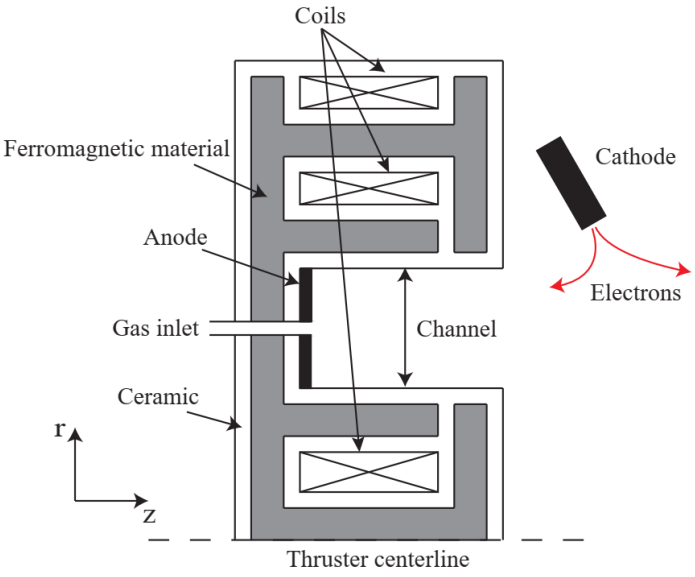

Figure 1. Schematic of the Hall thruster cross-section.

Geometrically, the thruster is symmetrically distributed about the central cylindrical axis. For the sake of analysis, a cylindrical coordinate system (*r, θ, z*) is established as follows: the origin is set at the center of the thruster's bottom face; the radial direction aligns with the radius of the base; the axial direction points perpendicularly upward from the base; and the toroidal direction circulates the axial direction.

According to Maxwell's equations, the magnetic field of the Hall thruster satisfies the following equations:

$$\nabla \cdot \boldsymbol{B} = 0 \tag{1}$$

$$\nabla \times \frac{\boldsymbol{B}}{\mu_r} = \mu_0 \boldsymbol{J} \tag{2}$$

where $\boldsymbol{B}$ is the magnetic field, $\boldsymbol{J}$ is the current density, μ_0 is the vacuum permeability, and μ_r is the relative permeability. Within ferromagnetic regions, the relative permeability exhibits a dependence on the magnetic field strength. For instance, the magnetization curve for a specific material is depicted in **Figure 2**. The relative permeability in these regions is derived from the corresponding magnetization curve, whereas it is set to unity in non-ferromagnetic regions.

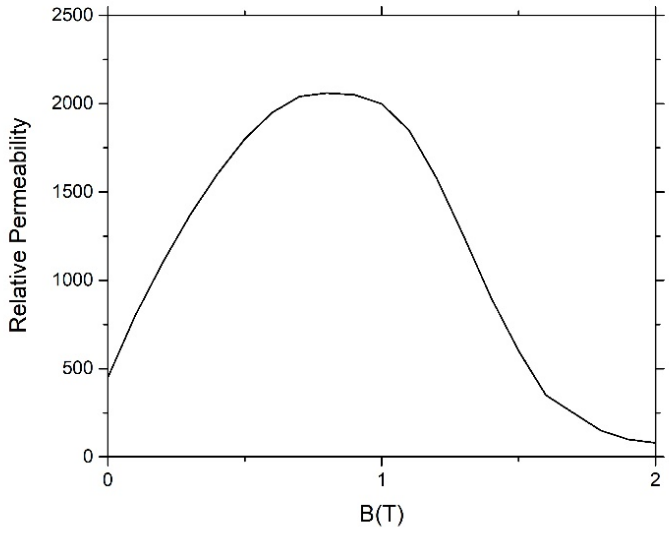

Figure 2. Magnetization curve of a ferromagnetic material.

It is evident from Equation (1) that the curl of the magnetic vector potential $\boldsymbol{A}$ can be used to express the magnetic field $\boldsymbol{B}$:

$$\boldsymbol{B} = \nabla \times \boldsymbol{A} \tag{3}$$

The magnetic vector potential $\boldsymbol{A}$ in the cylindrical coordinate system (*r, θ, z*) can be written as follows:

$$\boldsymbol{A} = A_r \boldsymbol{e}_r + A_\theta \boldsymbol{e}_\theta + A_z \boldsymbol{e}_z \tag{4}$$

Due to the axial symmetry of the Hall thruster's magnetic field (i.e., $\partial/\partial\theta = 0$), the magnetic vector potential $\boldsymbol{A}$ depends only on the coordinates (*r, z*) and possesses only a

toroidal (θ) component. As a result, the magnetic vector potential $\boldsymbol{A}$ can be reduced to

$$\boldsymbol{A} = A_\theta(r, z)\boldsymbol{e}_\theta \tag{5}$$

where A_θ is the toroidal component of the magnetic vector potential.

Substituting Equation (5) into Equation (3), we have

$$\boldsymbol{B} = -\frac{\partial A_\theta}{\partial z}\boldsymbol{e}_r + \frac{1}{r}\frac{\partial}{\partial r}(rA_\theta)\boldsymbol{e}_z \tag{6}$$

that is,

$$B_r = -\frac{\partial A_\theta}{\partial z} \tag{7}$$

$$B_\theta = 0 \tag{8}$$

$$B_z = \frac{1}{r}\frac{\partial}{\partial r}(rA_\theta) \tag{9}$$

where B_r, B_θ, and B_z are the radial, toroidal, and axial components of the magnetic field, respectively.

Substituting Equation (6) into Equation (2), it can be obtained

$$-\frac{\partial}{\partial r}\left[\frac{1}{\mu_r r}\frac{\partial}{\partial r}(rA_\theta)\right] - \frac{\partial}{\partial z}\left(\frac{1}{\mu_r}\frac{\partial A_\theta}{\partial z}\right) = \mu_0 J_\theta \tag{10}$$

where J_θ is the toroidal component of the current density.

Theoretically, the solution domain extends to the entire infinite region. Since the electromagnetic sources are confined to a finite region, the field quantities must decay as the distance increases. Therefore, a Dirichlet boundary condition is applied at infinity, where the magnetic vector potential vanishes. Consequently, Equation (10) has the following boundary condition as

$$r \to \infty, \quad z \to \pm\infty, \quad A_\theta = 0 \tag{11}$$

The model of the magnetic field in the Hall thruster is composed of Equations (7)–(10), with the boundary condition of Equation (11).

If μ_r and J_θ are known, Equation (10) can be used to determine A_θ under the previously mentioned boundary condition. The magnetic field $\boldsymbol{B}$ is obtained by substituting A_θ into Equation (6). Nevertheless, since the relative permeability in the ferromagnetic material is a nonlinear function of the magnetic field and its coefficient exhibits discontinuities in the solution domain, the solution process is a significant challenge.

3. Numerical approach

Since computers cannot process infinite regions, a finite computational domain must be defined. The boundaries of this domain must be situated sufficiently far from the thruster to ensure that the artificial boundaries do not distort the magnetic field solution. As illustrated in **Figure 3**, the computational domain is established as a rectangular region in the (*r, z*) plane of a cylindrical coordinate system.

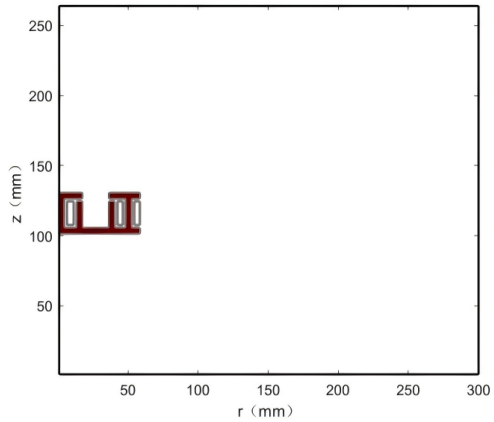

Figure 3. Computational domain setup for magnetic field simulation.

Extensive numerical tests indicate that when the domain area exceeds 20 times the cross-sectional area of the Hall thruster, the influence of boundary conditions becomes negligible. Based on this finding, the computational domain in the present work is defined as 40 times the thruster's cross-sectional area to ensure a sufficient safety margin. This configuration guarantees that the boundaries are far removed from the high-gradient regions, thereby ensuring the accuracy of the magnetic field results within both the channel and the plume.

The computational domain of this work uses a uniform staggered mesh with a spatial step size of h in both the r-direction and z-direction. In this finite difference framework, a staggered arrangement is utilized to enhance numerical robustness. Specifically, scalar properties such as magnetic permeability (μ_r) and source terms like current density (J_θ) are assigned to the cell centers. Conversely, the vector potential components (A_θ) are discretized at the mesh nodes. This configuration ensures that material properties represent the average value within a control volume, while the field gradients are calculated precisely at the boundaries, effectively preventing numerical oscillations.

The finite difference method is used to numerically discretize Equation (10) on this mesh. The first term on the left side of Equation (10) is discretized as

$$-\frac{2}{\widehat{\mu}_3}\frac{1}{r_{i+\frac{1}{2}}}\frac{r_{i+1}(A_\theta)_{i+1,j}-r_i(A_\theta)_{i,j}}{h^2}+\frac{2}{\widehat{\mu}_2}\frac{1}{r_{i-\frac{1}{2}}}\frac{r_i(A_\theta)_{i,j}-r_{i-1}(A_\theta)_{i-1,j}}{h^2} \tag{12}$$

The second term on the left side of Equation (10) is discretized as

$$-\frac{2}{\widehat{\mu}_4}\frac{(A_\theta)_{i,j+1}-(A_\theta)_{i,j}}{h^2}+\frac{2}{\widehat{\mu}_1}\frac{(A_\theta)_{i,j}-(A_\theta)_{i,j-1}}{h^2} \tag{13}$$

The term on the right side of Equation (10) is discretized as

$$\frac{\mu_0}{4}\left[(J_\theta)_{i-\frac{1}{2},j-\frac{1}{2}}+(J_\theta)_{i-\frac{1}{2},j+\frac{1}{2}}+(J_\theta)_{i+\frac{1}{2},j+\frac{1}{2}}+(J_\theta)_{i+\frac{1}{2},j-\frac{1}{2}}\right] \tag{14}$$

where

$$\widehat{\mu}_1=(\mu_r)_{i+\frac{1}{2},j-\frac{1}{2}}+(\mu_r)_{i-\frac{1}{2},j-\frac{1}{2}},$$

$$\widehat{\mu}_2=(\mu_r)_{i-\frac{1}{2},j+\frac{1}{2}}+(\mu_r)_{i-\frac{1}{2},j-\frac{1}{2}},$$

$$\widehat{\mu}_3 = (\mu_r)_{i+\frac{1}{2},j+\frac{1}{2}} + (\mu_r)_{i+\frac{1}{2},j-\frac{1}{2}} ,$$

$$\widehat{\mu}_4 = (\mu_r)_{i+\frac{1}{2},j+\frac{1}{2}} + (\mu_r)_{i-\frac{1}{2},j+\frac{1}{2}} .$$

From Equations (12)–(14), we obtain

$$-A_{ij}(A_\theta)_{i,j-1} - B_{ij}(A_\theta)_{i-1,j} + C_{ij}(A_\theta)_{i,j} - D_{ij}(A_\theta)_{i+1,j} - E_{ij}(A_\theta)_{i,j+1} = F_{ij} \quad (15)$$

where

$$A_{ij} = \frac{1}{\widehat{\mu}_1} \quad (16)$$

$$B_{ij} = \frac{r_{i-1}}{r_{i-\frac{1}{2}}} \frac{1}{\widehat{\mu}_2} \quad (17)$$

$$C_{ij} = \frac{1}{\widehat{\mu}_1} + \frac{r_i}{r_{i-\frac{1}{2}}} \frac{1}{\widehat{\mu}_2} + \frac{r_i}{r_{i+\frac{1}{2}}} \frac{1}{\widehat{\mu}_3} + \frac{1}{\widehat{\mu}_4} \quad (18)$$

$$D_{ij} = \frac{r_{i+1}}{r_{i+\frac{1}{2}}} \frac{1}{\widehat{\mu}_3} \quad (19)$$

$$E_{ij} = \frac{1}{\widehat{\mu}_4} \quad (20)$$

$$F_{ij} = \frac{\mu_0 h^2}{8} \left[(J_\theta)_{i-\frac{1}{2},j-\frac{1}{2}} + (J_\theta)_{i-\frac{1}{2},j+\frac{1}{2}} + (J_\theta)_{i+\frac{1}{2},j+\frac{1}{2}} + (J_\theta)_{i+\frac{1}{2},j-\frac{1}{2}} \right] \quad (21)$$

Equation (7) is discretized as

$$(B_r)_{ij} = -\frac{(A_\theta)_{i,j+1} - (A_\theta)_{i,j-1}}{2h} \quad (22)$$

$$(B_r)_{i0} = -\frac{-3(A_\theta)_{i0} + 4(A_\theta)_{i1} - (A_\theta)_{i2}}{2h} \quad (23)$$

$$(B_r)_{in_z} = -\frac{(A_\theta)_{i,n_z-2} - 4(A_\theta)_{i,n_z-1} + 3(A_\theta)_{i,n_z}}{2h} \quad (24)$$

where $i = 0, 1, \ldots, n_r$ and $j = 1, 2, \ldots, n_z - 1$.

Given the singularity of Equation (9) at $r = 0$, it is recast as follows:

$$B_z = \begin{cases} 2\frac{\partial A_\theta}{\partial r}, & r = 0 \\ \frac{\partial A_\theta}{r} + \frac{\partial A_\theta}{\partial r}, & r > 0 \end{cases} \quad (25)$$

Equation (25) is discretized as

$$(B_z)_{ij} = \frac{1}{r_i} \frac{r_{i+1}(A_\theta)_{i+1,j} - r_{i-1}(A_\theta)_{i-1,j}}{2h} \quad (26)$$

$$(B_z)_{0j} = \frac{-3(A_\theta)_{0j} + 4(A_\theta)_{1j} - (A_\theta)_{2j}}{h} \quad (27)$$

$$(B_z)_{n_r j} = \frac{1}{r_{n_r}} \frac{r_{n_r-2}(A_\theta)_{i,n_r-2} - 4r_{n_r-1}(A_\theta)_{i,n_r-1} + 3r_{n_r}(A_\theta)_{i,n_r}}{2h} \quad (28)$$

where $i = 1, 2, \ldots, n_r - 1$ and $j = 0, 1, \ldots, n_z$.

The magnetic field is

$$B_{ij} = \sqrt{(B_r)_{ij}^2 + (B_z)_{ij}^2} \tag{29}$$

where $i = 0, 1, \ldots, n_r$ and $j = 0, 1, \ldots, n_z$.

The system of Equation (15) is a nonlinear system that can be solved using the following iterative method in **Algorithm 1**.

Algorithm 1 Standard Iterative Model

1. Enter the spatial mesh pitch, geometry parameters and ampere-turns of coils;
2. Calculate F_{ij} using Equation (21), where $i = 1, 2, \ldots, n_r - 1$ and $j = 1, 2, \ldots, n_z - 1$;
3. Let $(A_\theta)_{ij}^{(0)} = 0$, where $i = 0, 1, \ldots, n_r$ and $j = 0, 1, \ldots, n_z$;
4. Calculate $(B_r)_{ij}^{(0)}$,$(B_z)_{ij}^{(0)}$,$(B)_{ij}^{(0)}$ using Equations (22)–(24) and (26)–(29);
5. Calculate the magnetic permeability $(\mu_r)_{i-\frac{1}{2},j-\frac{1}{2}}^{(0)}$ based on the $\mu - B$ curve, where $i = 1, \ldots, n_r$ and $j = 1, \ldots, n_z$;
6. Calculate $A_{ij}^{(0)}$,$B_{ij}^{(0)}$,$C_{ij}^{(0)}$,$D_{ij}^{(0)}$, and $E_{ij}^{(0)}$ using Equations (16)–(20), where $i = 1, 2, \ldots, n_r - 1$ and $j = 1, 2, \ldots, n_z - 1$;
7. Let $(A_\theta)_{ij}^{(1)} = 0$, where $i = 0, n_r$ and $j = 0, n_z$;
8. Let $(A_\theta)_{ij}^{(1)} = \frac{A_{ij}^{(0)}(A_\theta)_{i,j-1}^{(0)} + B_{ij}^{(0)}(A_\theta)_{i-1,j}^{(0)} + D_{ij}^{(0)}(A_\theta)_{i+1,j}^{(0)} + E_{ij}^{(0)}(A_\theta)_{i,j+1}^{(0)} + F_{ij}}{C_{ij}^{(0)}}$, where $i = 1, 2, \ldots, n_r - 1$ and $j = 1, 2, \ldots, n_z - 1$;
9. If $\sqrt{\frac{\sum_{ij}[(A_\theta)_{ij}^{(1)} - (A_\theta)_{ij}^{(0)}]^2}{\sum_{ij}[(A_\theta)_{ij}^{(1)}]^2}} > \varepsilon_A$, replace $(A_\theta)_{ij}^{(1)}$ with $(A_\theta)_{ij}^{(0)}$ and go back to step 7, where ε_A is the set error limit for A_θ, $i = 1, 2, \ldots, n_r - 1$ and $j = 1, 2, \ldots, n_z - 1$;
10. Calculate $(B_r)_{ij}^{(1)}$,$(B_z)_{ij}^{(1)}$,$(B)_{ij}^{(1)}$ using Equations (22)–(24) and (26)–(29);
11. Calculate the magnetic permeability $(\mu_r)_{i-\frac{1}{2},j-\frac{1}{2}}^{(1)}$ based on the $\mu - B$ curve, where $i = 1, \ldots, n_r$ and $j = 1, \ldots, n_z$;
12. If $\sqrt{\frac{\sum_{ij}[(\mu_r)_{i-\frac{1}{2},j-\frac{1}{2}}^{(1)} - (\mu_r)_{i-\frac{1}{2},j-\frac{1}{2}}^{(0)}]^2}{\sum_{ij}[(\mu_r)_{i-\frac{1}{2},j-\frac{1}{2}}^{(1)}]^2}} > \varepsilon_\mu$, replace $(\mu_r)_{i-\frac{1}{2},j-\frac{1}{2}}^{(1)}$ with $(\mu_r)_{i-\frac{1}{2},j-\frac{1}{2}}^{(0)}$ and go back to step 6, where ε_μ is the set error limit for μ_r, $i = 1, 2, \ldots, n_r$ and $j = 1, 2, \ldots, n_z$;
13. Output the calculation results;
14. End.

Steps 8 and 9 of the aforementioned iterative method involve solving the boundary value problem of an elliptic partial differential equation by determining the magnetic potential based on a given relative permeability. According to finite difference theory, this iteration converges. However, the relative permeability is a nonlinear function of the magnetic field rather than a constant. Although the relative permeability is updated during the sixth through twelfth iterations of the aforementioned method, there is currently no theoretical proof guaranteeing the convergence of this iterative solution. To address this issue and achieve convergence in the magnetic potential iteration, we attempted to incorporate Aitken extrapolation into the previous iterative method. This is how the Aitken extrapolation formula is obtained:

Let $\{x_k\}$ converge linearly to α, that is,

$$\lim_{k\to\infty} \frac{x_{k+1} - \alpha}{x_k - \alpha} = c \tag{30}$$

where $|c| < 1$.

When k is sufficiently large, we have

$$\frac{x_{k+1} - \alpha}{x_k - \alpha} \approx \frac{x_{k+2} - \alpha}{x_{k+1} - \alpha} \tag{31}$$

Let

$$\frac{x_{k+1}-\bar{x}_{k+3}}{x_k-\bar{x}_{k+3}}=\frac{x_{k+2}-\bar{x}_{k+3}}{x_{k+1}-\bar{x}_{k+3}} \tag{32}$$

Solving Equation (32), we obtain

$$\bar{x}_{k+3}=x_k-\frac{(x_{k+1}-x_{k+2})^2}{x_{k+2}-2x_{k+1}+x_k} \tag{33}$$

This is the Aitken extrapolation formula.

The Aitken method assumes the sequence converges linearly. In our magnetic field problem, as the solution approaches the steady state, the nonlinearity of the $\mu-B$ curve becomes less significant, and the iteration behaves like a linear fixed-point iteration. Under this condition, Aitken extrapolation is effective in accelerating the convergence.

Based on the mathematical derivation above, the implementation of the Aitken acceleration within the magnetic potential iteration can be formalized, as seen in **Algorithm 2**.

Algorithm 2 Iterative Method with Aitken Extrapolation

1. Enter the spatial mesh pitch, geometry parameters and ampere-turns of coils;
2. Calculate F_{ij} using Equation (21), where $i=1,2,\ldots,n_r-1$ and $j=1,2,\ldots,n_z-1$;
3. Let $(A_\theta)_{ij}^{(0)}=0$, where $i=0,1,\ldots,n_r$ and $j=0,1,\ldots,n_z$;
4. Calculate $(B_r)_{ij}^{(0)}$,$(B_z)_{ij}^{(0)}$,$(B)_{ij}^{(0)}$ using Equations (22)–(24) and (26)–(29);
5. Calculate the magnetic permeability $(\mu_r)_{i-\frac{1}{2},j-\frac{1}{2}}^{(0)}$ based on the $\mu-B$ curve, where $i=1,\ldots,n_r$ and $j=1,\ldots,n_z$;
6. Calculate $A_{ij}^{(0)}$,$B_{ij}^{(0)}$,$C_{ij}^{(0)}$,$D_{ij}^{(0)}$, and $E_{ij}^{(0)}$ using Equations (16)–(20), where $i=1,2,\ldots,n_r-1$ and $j=1,2,\ldots,n_z-1$;
7. Let $(A_\theta)_{ij}^{(1)}=0$, where $i=0,n_r$ and $j=0,n_z$;
8. Let $(A_\theta)_{ij}^{(1)}=\frac{A_{ij}^{(0)}(A_\theta)_{i,j-1}^{(0)}+B_{ij}^{(0)}(A_\theta)_{i-1,j}^{(0)}+D_{ij}^{(0)}(A_\theta)_{i+1,j}^{(0)}+E_{ij}^{(0)}(A_\theta)_{i,j+1}^{(0)}+F_{ij}}{C_{ij}^{(0)}}$, where $i=1,2,\ldots,n_r-1$ and $j=1,2,\ldots,n_z-1$;
9. If $\sqrt{\frac{\sum_{ij}[(A_\theta)_{ij}^{(1)}-(A_\theta)_{ij}^{(0)}]^2}{\sum_{ij}[(A_\theta)_{ij}^{(1)}]^2}}>\varepsilon_A$, replace $(A_\theta)_{ij}^{(1)}$ with $(A_\theta)_{ij}^{(0)}$ and go back to step 7, where ε_A is the set error limit for A_θ, $i=1,2,\ldots,n_r-1$ and $j=1,2,\ldots,n_z-1$;
10. Calculate $(B_r)_{ij}^{(1)}$,$(B_z)_{ij}^{(1)}$,$(B)_{ij}^{(1)}$ using Equations (22)–(24) and (26)–(29);
11. Calculate the magnetic permeability $(\mu_r)_{i-\frac{1}{2},j-\frac{1}{2}}^{(1)}$ based on the $\mu-B$ curve, where $i=1,\ldots,n_r$ and $j=1,\ldots,n_z$;
12. Calculate $A_{ij}^{(1)}$,$B_{ij}^{(1)}$,$C_{ij}^{(1)}$,$D_{ij}^{(1)}$, and $E_{ij}^{(1)}$ using Equations (16)–(20), where $i=1,2,\ldots,n_r-1$ and $j=1,2,\ldots,n_z-1$;
13. Let $(A_\theta)_{ij}^{(2)}=0$, where $i=0,n_r$ and $j=0,n_z$;
14. Let $(A_\theta)_{ij}^{(2)}=\frac{A_{ij}^{(1)}(A_\theta)_{i,j-1}^{(1)}+B_{ij}^{(1)}(A_\theta)_{i-1,j}^{(1)}+D_{ij}^{(1)}(A_\theta)_{i+1,j}^{(1)}+E_{ij}^{(1)}(A_\theta)_{i,j+1}^{(1)}+F_{ij}}{C_{ij}^{(1)}}$, where $i=1,2,\ldots,n_r-1$ and $j=1,2,\ldots,n_z-1$;
15. If $\sqrt{\frac{\sum_{ij}[(A_\theta)_{ij}^{(2)}-(A_\theta)_{ij}^{(1)}]^2}{\sum_{ij}[(A_\theta)_{ij}^{(2)}]^2}}>\varepsilon_A$, replace $(A_\theta)_{ij}^{(2)}$ with $(A_\theta)_{ij}^{(1)}$ and go back to step 13, where ε_A is the set error limit for A_θ, $i=1,2,\ldots,n_r-1$ and $j=1,2,\ldots,n_z-1$;
16. Calculate $(B_r)_{ij}^{(2)}$,$(B_z)_{ij}^{(2)}$,$(B)_{ij}^{(2)}$ using Equations (22)–(24) and (26)–(29);
17. Calculate the magnetic permeability $(\mu_r)_{i-\frac{1}{2},j-\frac{1}{2}}^{(2)}$ based on the $\mu-B$ curve, where $i=1,\ldots,n_r$ and $j=1,\ldots,n_z$;
18. Apply the Aitken extrapolation correction,
$(\mu_r)_{i-\frac{1}{2},j-\frac{1}{2}}^{(3)}=(\mu_r)_{i-\frac{1}{2},j-\frac{1}{2}}^{(0)}-\frac{\left[(\mu_r)_{i-\frac{1}{2},j-\frac{1}{2}}^{(1)}-(\mu_r)_{i-\frac{1}{2},j-\frac{1}{2}}^{(2)}\right]^2}{(\mu_r)_{i-\frac{1}{2},j-\frac{1}{2}}^{(2)}-2(\mu_r)_{i-\frac{1}{2},j-\frac{1}{2}}^{(1)}+(\mu_r)_{i-\frac{1}{2},j-\frac{1}{2}}^{(0)}}$, where $i=1,\ldots,n_r$ and $j=1,\ldots,n_z$;
19. If $\sqrt{\frac{\sum_{ij}[(\mu_r)_{i-\frac{1}{2},j-\frac{1}{2}}^{(3)}-(\mu_r)_{i-\frac{1}{2},j-\frac{1}{2}}^{(0)}]^2}{\sum_{ij}[(\mu_r)_{i-\frac{1}{2},j-\frac{1}{2}}^{(3)}]^2}}>\varepsilon_\mu$, replace $(\mu_r)_{i-\frac{1}{2},j-\frac{1}{2}}^{(3)}$ with $(\mu_r)_{i-\frac{1}{2},j-\frac{1}{2}}^{(0)}$ and go back to step 6, where ε_μ is the set error limit for μ_r, $i=1,2,\ldots,n_r$ and $j=1,2,\ldots,n_z$;
20. Output the calculation results;
21. End.

This paper proposes two iterative algorithms, designated as **Algorithm 1** and **Algorithm 2**. **Algorithm 2** incorporates Aitken extrapolation, whereas **Algorithm 1**

operates without this enhancement. Both algorithms feature a nested loop structure to handle the nonlinearity: the inner iteration solves the field equation for the magnetic vector potential (A_θ) with a fixed relative permeability (μ_r), while the outer iteration updates the relative permeability (μ_r) distribution according to the current magnetic field ($\boldsymbol{B}$) distribution.

4. Results and discussion

4.1. Numerical verification and model configuration

4.1.1. Mathematical consistency and mesh convergence

To ensure the mathematical consistency of the proposed scheme, the numerical residuals were first evaluated by calculating the difference between the right-hand side and left-hand side of the discrete Equation (15). **Table 1** summarizes the statistical metrics of the residuals. The RMSE is 9.37×10^{-12} and the E_{max} is 3.15×10^{-10}. Furthermore, the ME is calculated to be -7.36×10^{-13}. This near-zero mean value confirms that the numerical errors are unbiased and randomly distributed, rather than accumulating in a specific direction.

Table 1. Statistical metrics of the numerical residuals.

Metric	Value
Root Mean Square Error (RMSE)	9.37×10^{-12}
Mean Absolute Error (MAE)	7.4×10^{-13}
Maximum Absolute Error (E_{max})	3.15×10^{-10}
Mean Error (ME)	-7.36×10^{-13}

Subsequently, a mesh refinement study was conducted to evaluate the influence of mesh resolution on the accuracy of the magnetic field solution and to establish a balance between computational accuracy and cost. Three meshes of increasing resolution—coarse, medium, and fine—were used for the overall magnetic field calculation. The axial magnetic field profile through the magnetic null point was then extracted from each solution for comparative analysis.

Figure 4 presents the axial magnetic field profiles obtained with the three meshes. The curves for all three resolutions overlap closely, with only minor deviations observable in the region of the peak field. This strong qualitative agreement indicates that the solution has effectively converged and is largely insensitive to further mesh refinement.

To quantify the convergence behavior, the RMSE between adjacent mesh levels was calculated, using the magnetic field range of the fine mesh solution for normalization. The results are summarized in **Table 2**. The relative error from the coarse to the medium mesh is 2.14%, which decreases to 1.28% from the medium to the fine mesh. This decreasing trend confirms that the solution is indeed converging with mesh refinement.

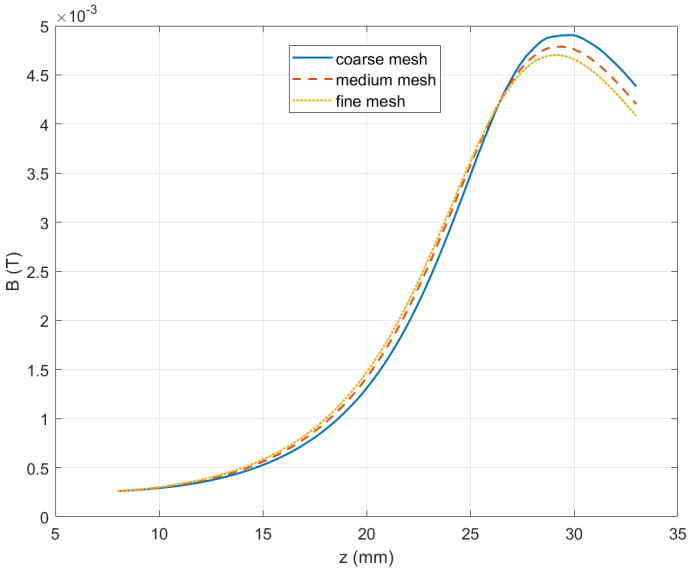

Figure 4. The axial magnetic field profiles through the magnetic null point.

Table 2. Quantitative errors between adjacent mesh levels.

Comparison	RMSE (T)	Relative error (%)
Coarse → Medium	9.50×10^{-3}	2.14
Medium → Fine	5.70×10^{-5}	1.28

While further mesh refinement reduces the numerical error, it comes at a significant increase in computational cost. **Table 3** reports the computational time required by each mesh. Compared to the coarse mesh, the medium mesh is approximately 17.8 times slower, and the fine mesh is 257.8 times slower, while only reducing the relative error by less than one percentage point.

Table 3. Computational time for each mesh level.

Mesh level	Computational time (s)	Time ratio
Coarse	49.52	1.0×
Medium	884.98	17.8×
Fine	12,770.40	257.8×

Based on these results, mesh convergence is achieved, as the relative error decreases with mesh refinement while the magnetic field profiles remain nearly identical across all resolutions. Although further refinement reduces the numerical error, the marginal improvement from the coarse to the medium mesh does not justify the dramatically higher computational cost, as the medium mesh is 17.8 times slower and the fine mesh is 257.8 times slower than the coarse mesh. Therefore, the coarse mesh is considered sufficient for all subsequent analyses in this work, as it provides a converged and accurate solution with a relative error under 2.2% while maintaining high computational efficiency.

4.1.2. Hall thruster geometry and computational setup

The numerical model is established based on a miniature Hall thruster. The specific geometric dimensions are as follows: a radial length of 60 mm, an inner diameter of 19 mm, an outer diameter of 36 mm, and a channel width of 17 mm. The channel length measures 25 mm, with a total axial length of 33 mm. The magnetic field calculation domain encompasses an area forty times that of the thruster's cross-section.

The magnetic circuit incorporates the non-linear characteristics of the ferromagnetic core, as illustrated in the provided μ-B curve (**Figure 2**). The magnetic field is generated by a specific coil arrangement consisting of three solenoids (as shown in **Figure 1**), where the excitation for each case is defined by the specific Ampere-turns applied to each coil.

4.1.3. Algorithm implementation and convergence criteria

In the computational results, the number of outer-loop iterations is recorded, while the inner-loop iterations are set to a fixed limit. This upper limit of 3,000,000 cycles is established as a definitive divergence threshold. Its primary purpose is to prevent infinite loops and to rigorously test the robustness of the algorithms under extreme non-linear conditions, rather than reflecting the typical convergence speed in standard operations. As the following cases demonstrate, this cap is sufficiently high to capture both convergence and divergence behaviors.

This section employs **Algorithms 1** and **2** to compute the iteration time and magnetic fields under three distinct sets of coil ampere-turns. The relative performance of the two methods is evaluated by comparing their convergence trends. To verify the physical validity of the model, the magnetic flux distributions and axial field components are analyzed to confirm the presence of a magnetic null point and the characteristic field topology required for Hall thrusters.

The convergence behavior of the non-linear magnetic field calculation is closely tied to the specific operating conditions of the Hall thruster. The magnetic field within the channel typically ranges from 0.01 T to 0.04 T. As illustrated in the relative permeability curve (**Figure 2**), this range corresponds to distinct excitation levels of the ferromagnetic material's magnetization process.

Our numerical tests reveal a distinct performance difference between the standard fixed-point iteration and the Aitken method across this operational range. In the lower field region, where the magnetic excitation is mild, the system responds predictably. The standard fixed-point iteration is generally stable and convergent. However, in this regime, the Aitken method—while providing a robust alternative—may not always yield a speed advantage due to its additional computational steps.

In contrast, in the higher field region, where the excitation intensity is high, the non-linearity of the material properties becomes more pronounced, leading to strong coupling effects. Under these demanding conditions, the standard iteration often fails to converge due to oscillations. The proposed Aitken acceleration method is crucial here, as it effectively suppresses these oscillations by extrapolating the sequence of permeability updates and thereby enables convergence where the standard method fails.

This analysis explains the comparative results of **Algorithms 1** and **2** presented

in the following sections. While the Aitken method may incur a slight overhead in the low-excitation region, its ability to improve stability in the high-field region makes it the preferred choice for the robust simulation of Hall thrusters.

The following sections present the computational performance of these two algorithms under three distinct excitation conditions.

4.2. Performance analysis under different excitation regimes

4.2.1. Case 1: Low-excitation regime

Figures 5 and **6** illustrate the magnetic field characteristics under low excitation of 50 A, 60 A and 50 A. The magnetic flux distribution clearly identifies the location of the magnetic null point, and the axial field profile exhibits the characteristic topology required for electron confinement. This confirms the physical fidelity of the model.

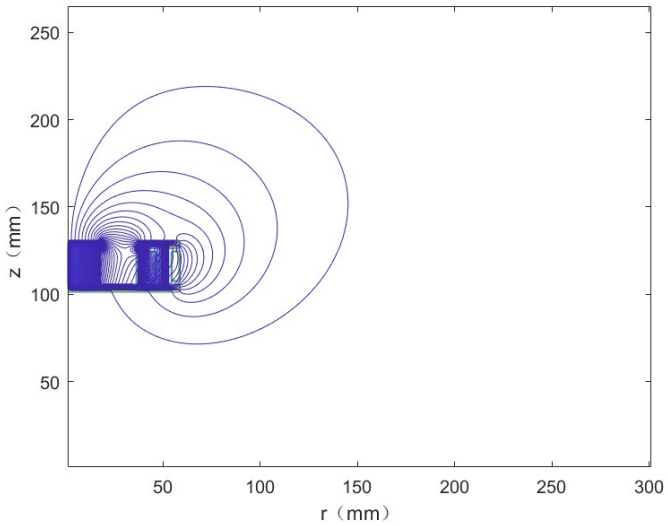

Figure 5. The magnetic flux distribution (low-excitation regime).

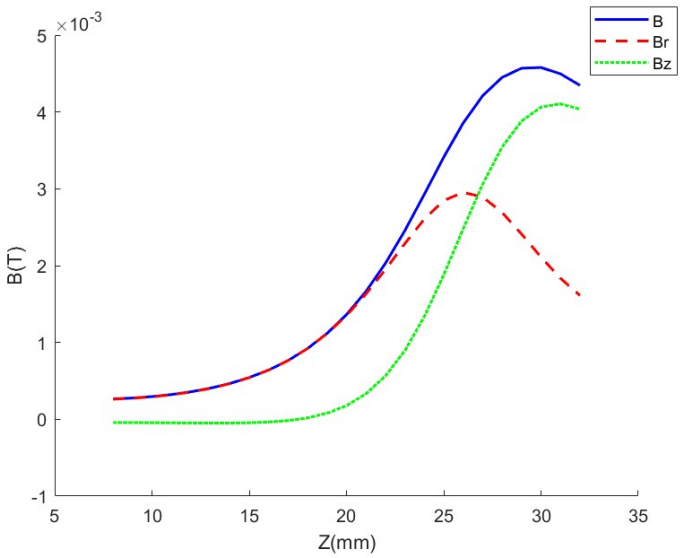

Figure 6. The axial magnetic field and its components profile through the magnetic null point (low-excitation regime).

Based on this physical configuration, **Figure 7** illustrates the convergence history where the maximum magnetic flux density in the channel reaches 0.0132 T. To further evaluate the computational efficiency, the time cost per iteration for both methods is plotted in **Figure 8**.

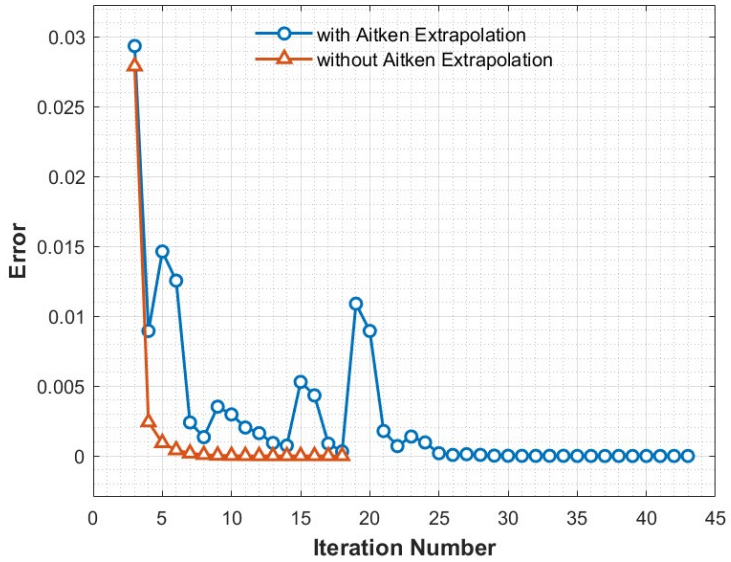

Figure 7. Convergence trend (low-excitation regime).

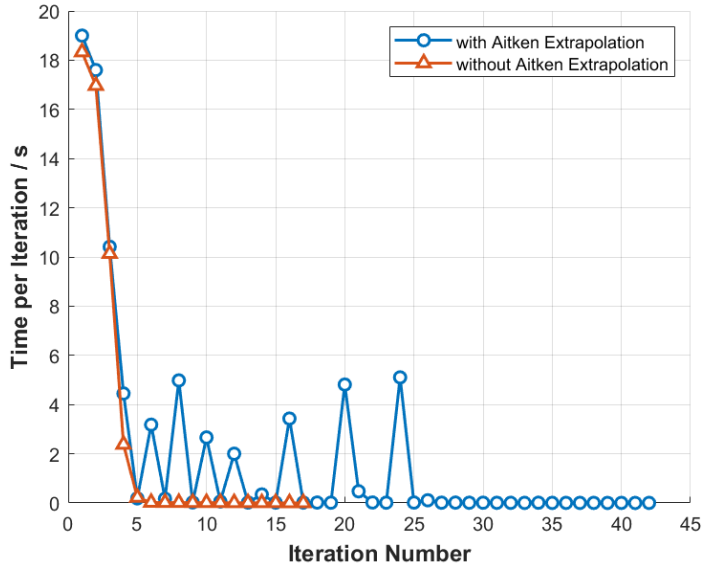

Figure 8. Comparison of computational time per iteration (low-excitation regime).

Algorithm 1 exhibits a smooth, monotonic decrease in error, rapidly converging to the tolerance within 18 iterations. As shown in **Figure 8**, the computational cost per step for **Algorithm 1** is consistently low and stable, resulting in a total computation time of 49.52 s. This stability indicates that for magnetic field configurations with mild nonlinearity, the standard fixed-point iteration is naturally robust and highly efficient.

In contrast, **Algorithm 2** displays a fluctuating convergence path. While the acceleration technique aims to speed up the process, **Figure 8** reveals that the Aitken extrapolation introduces significant computational overhead and instability. The time

per iteration for **Algorithm 2** is not only highly oscillatory but also incurs frequent spikes due to the additional extrapolation calculations. These fluctuations correspond to the overshooting effects that destabilize the iteration process. Consequently, **Algorithm 2** requires 43 iterations and 82.43 s to complete the computation. This result suggests that applying acceleration techniques to mild nonlinearity problems can be counterproductive, as the overhead of the extrapolation calculation and the oscillatory behavior outweigh the speedup.

4.2.2. Case 2: Moderate-excitation regime

Figures 9 and **10** illustrate the magnetic field characteristics under a moderate excitation of 50 A, 150 A, and 50 A. The simulation results confirm that the magnetic topology maintains the required features, particularly regarding the location of the magnetic null point.

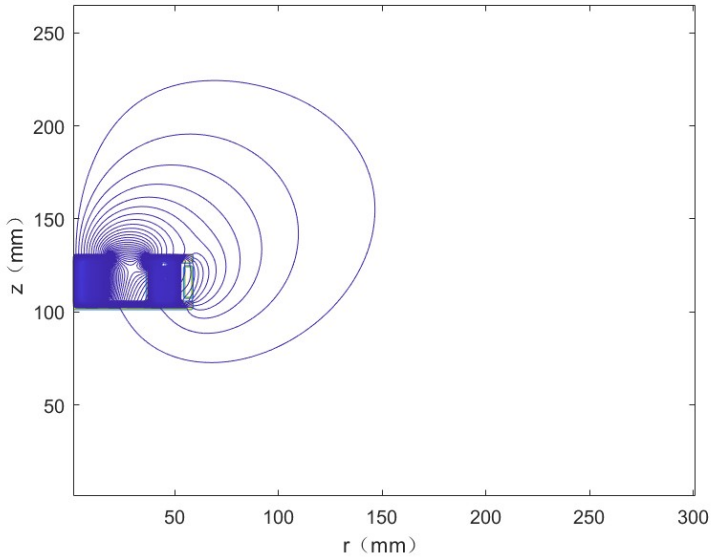

Figure 9. The magnetic flux distribution (moderate-excitation regime).

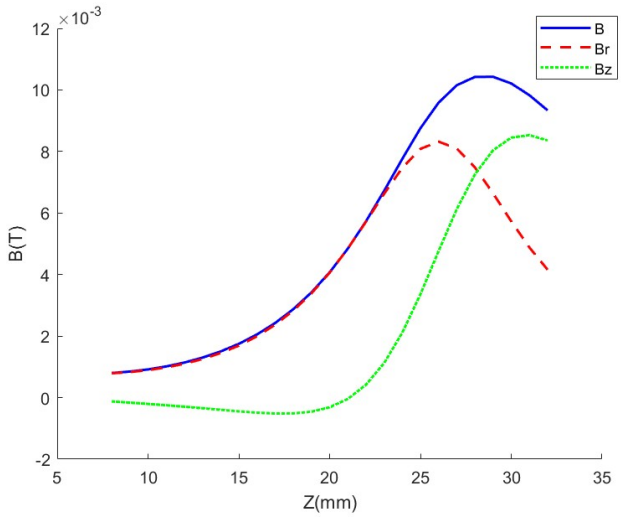

Figure 10. The axial magnetic field and its components profile through the magnetic null point (moderate-excitation regime).

Having validated the physical correctness of the model, we further analyze the computational efficiency required to obtain this solution. **Figure 11** illustrates the convergence history where the maximum magnetic flux density in the channel reaches 0.0344 T. To understand the underlying cost structure, the time per iteration is detailed in **Figure 12**.

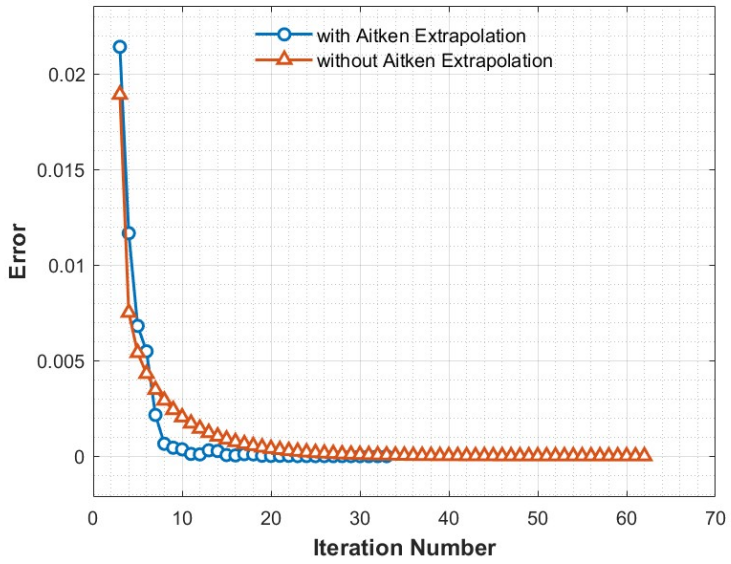

Figure 11. Convergence trend (moderate-excitation regime).

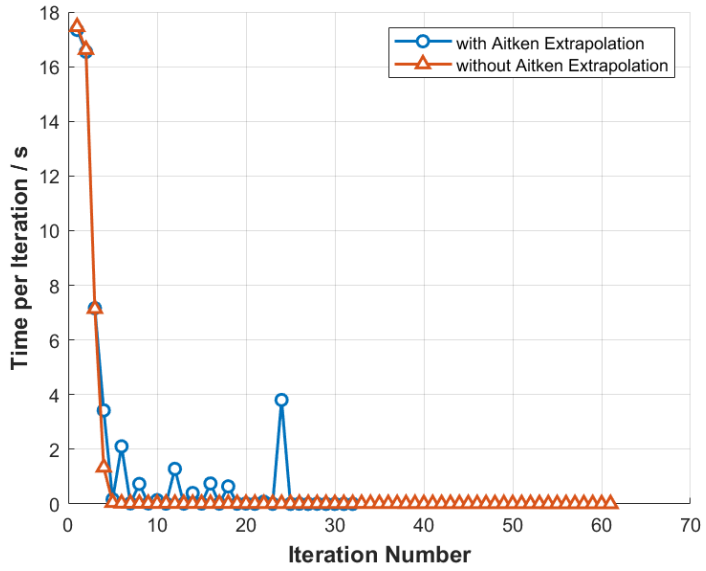

Figure 12. Comparison of computational time per iteration (moderate-excitation regime).

In this scenario, both algorithms successfully converge, but they exhibit a distinct trade-off between iteration count and computational cost per step. **Algorithm 2** accelerates the convergence rate significantly, reducing the iteration count to 33. However, as shown in **Figure 12**, the inclusion of Aitken extrapolation introduces additional computational overhead, resulting in a higher and more fluctuating time cost per iteration compared to the stable, minimal cost of **Algorithm 1**. Consequently, despite the fewer iterations, **Algorithm 2** requires a total of 58.26 s.

Conversely, **Algorithm 1** follows a slower, monotonic convergence path, requiring 62 iterations. Despite the higher iteration count, its computational efficiency per step is much higher due to the absence of extrapolation overhead, as evidenced by the consistently low time cost in **Figure 12**. As a result, **Algorithm 1** completes the task in only 42.85 s, demonstrating superior overall time efficiency even in scenarios with stronger magnetic nonlinearity.

4.2.3. Case 3: High-excitation regime

Figures 13 and **14** illustrate the magnetic field characteristics under a high-excitation winding configuration with ampere-turns of 50 A, 160 A, and 50 A. The results confirm that the magnetic field topology satisfies the design requirements, with the magnetic null point and peak intensity aligning with the expected operational parameters.

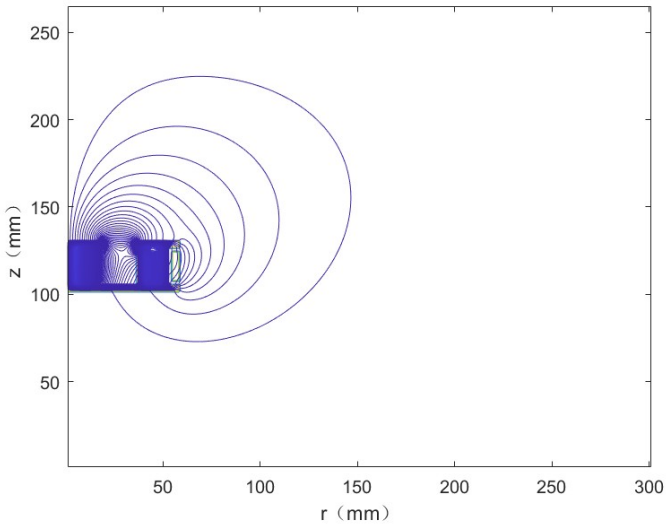

Figure 13. The magnetic flux distribution (high-excitation regime).

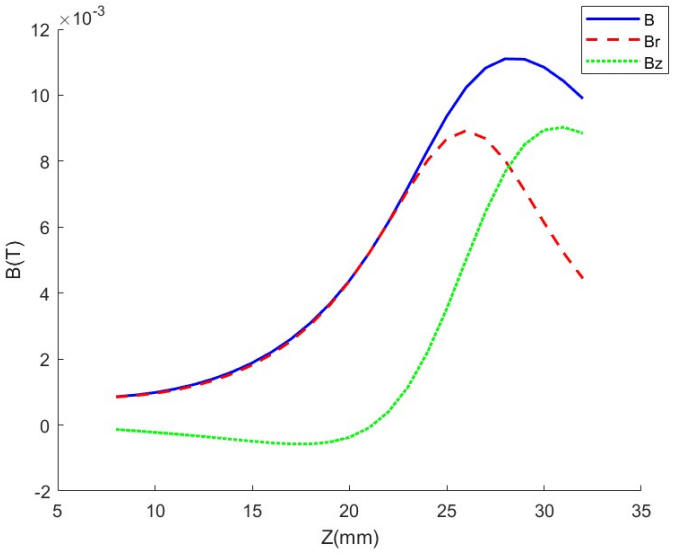

Figure 14. The axial magnetic field and its components profile through the magnetic null point (high-excitation regime).

Based on this physical configuration, **Figure 15** illustrates the convergence history where the maximum magnetic flux density in the channel reaches 0.0368 T. In this scenario, the high excitation current induces a strong magnetic nonlinearity, where the magnetic permeability (μ_r) varies drastically with the field distribution.

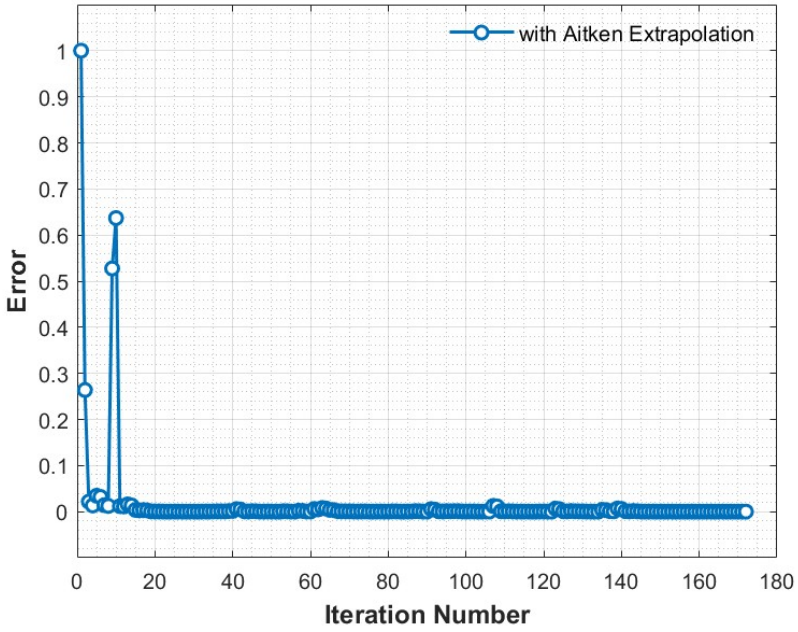

Figure 15. Convergence trend (high-excitation regime).

This strong nonlinearity poses a significant challenge for **Algorithm 1**. Without acceleration, the update scheme suffers from severe numerical oscillations, causing the error to diverge rather than diminish. The lack of damping or predictive correction in **Algorithm 1** renders it unstable under these conditions.

In contrast, **Algorithm 2** effectively stabilizes the calculation. By incorporating Aitken extrapolation, the algorithm suppresses these oscillations and successfully drives the error to the tolerance. Although it requires 172 iterations and 189.83 s to complete the computation, this result demonstrates that when standard iteration fails due to strong nonlinearity, Aitken extrapolation is essential for ensuring computational convergence, making **Algorithm 2** the only viable option for this specific operating condition.

4.3. Limitations and future work

Despite the promising results, there are two main limitations in this study that should be acknowledged. First, the numerical model relies on an ideal axisymmetric assumption. This simplification neglects potential toroidal asymmetries caused by manufacturing tolerances or discrete pole structures found in practical thrusters. Second, the current study treats the magnetic field in a decoupled manner, excluding the influence of the plasma-induced magnetic field. While this coupling is often negligible in low-to-moderate power regimes, it can become significant in high-power applications due to diamagnetic effects. Future work will focus on extending the model to three-dimensional geometries and incorporating self-consistent plasma-field

interactions to further enhance the simulation accuracy.

5. Conclusion

This paper presents an axisymmetric numerical model based on Maxwell's equations to address the challenge of solving nonlinear elliptic partial differential equations with discontinuous coefficients in Hall thruster magnetic field calculations. The model accounts for the nonlinear dependence of relative permeability on the magnetic field in ferromagnetic materials. By discretizing the governing equations on a uniform staggered mesh using the finite difference method, we developed a nested loop iterative framework. To enhance the robustness of the solution, an Aitken extrapolation formula was incorporated into the algorithm.

The rigorous verification process confirms the robustness of the proposed scheme. The residual analysis demonstrates that the numerical errors are unbiased with a Mean Error of approximately -7.36×10^{-13}. The results also show a Root Mean Square Error of 9.37×10^{-12} and a Maximum Absolute Error of 3.15×10^{-10}, indicating high numerical precision.

The mesh refinement study confirms that the magnetic field solution has converged, as the axial magnetic field profiles through the magnetic null point overlap closely across all three mesh resolutions. The relative error decreases from 2.14% (coarse to medium) to 1.28% (medium to fine), but this minor improvement comes at a dramatic increase in computational cost: the medium mesh is 17.8 times slower and the fine mesh is 257.8 times slower than the coarse mesh. Consequently, the coarse mesh is adopted for all subsequent simulations, as it offers a converged and accurate solution with a relative error under 2.2% while maintaining optimal computational efficiency.

The comparative analysis of the numerical methods reveals a distinct trade-off between efficiency and stability depending on the excitation level. In the low-excitation regime, the standard fixed-point iteration demonstrates superior computational efficiency, whereas the Aitken extrapolation introduces unnecessary computational overhead. However, in the high-excitation regime, the strong nonlinearity of the ferromagnetic material causes the standard iteration to diverge. Under these conditions, the proposed Aitken-accelerated algorithm becomes essential as it effectively suppresses oscillations and improves convergence, demonstrating its critical value for robust simulations under high-field conditions.

Furthermore, the physical validity of the model is confirmed by the resulting magnetic field topology. The computed magnetic flux distributions and axial field profiles near the magnetic null point align well with the design requirements for Hall thrusters. The successful reproduction of the magnetic null point location indicates that the proposed numerical approach is a reliable tool for the analysis and optimization of Hall thruster magnetic circuits.

Author contributions: Conceptualization, YL; methodology, YL; software, JL and YX; validation, JL; formal analysis, JL and YX; resources, YL; data curation, JL; writing—original draft preparation, JL; writing—review and editing, YL and YX;

visualization, JL. All authors have read and agreed to the published version of the manuscript.

Funding: This work received no external funding.

Institutional review board statement: Not applicable.

Informed consent statement: Not applicable.

Data availability statement: The data that support the findings of this study are available from the corresponding author upon reasonable request.

Conflict of interest: The authors declare no conflict of interest.

AI use statement: AI-based writing assistance, specifically Grammarly, was used to enhance the manuscript's language and formatting. The authors confirm that all scientific content and conclusions are original and accurately reflect their work.

References

1. Ren L, Wang Y, Jin L, et al. Effect of magnetic field strength on the performance characterization of a low-power wall-less Hall thruster. Vacuum. 2024; 220: 112820. doi: 10.1016/j.vacuum.2023.112820
2. Zubair J. Development of a 12.5kW Hall Thruster for the Advanced Electric Propulsion System. In: Proceedings of the AIAA Propulsion and Energy 2020 Forum; 24–28 August 2020; Online. doi: 10.2514/6.2020-3628
3. Singh S, Kumar S, Kumar Meena S, et al. Introduction to Plasma Based Propulsion System: Hall Thrusters. In: Matsuuchi K, Hasegawa H (editors). Propulsion - New Perspectives and Applications. IntechOpen; 2021. doi: 10.5772/intechopen.96916
4. Chhavi C, Walker MLR. Review of non-conventional Hall effect thrusters. Journal of Electric Propulsion. 2024; 3(1): 11. doi: 10.1007/s44205-024-00073-2
5. Ferreira JL, Martins AA, Miranda R, et al. Permanent magnet Hall thruster development for future Brazilian space missions. Computational and Applied Mathematics. 2016; 35(3): 711–726. doi: 10.1007/s40314-015-0286-4
6. Li Y, Wang W, Kong W, et al. Novel electromagnetic control method of propulsion performance and discharge oscillations in a wall-less Hall thruster. Chinese Journal of Aeronautics. 2026; 39(3): 103697. doi: 10.1016/j.cja.2025.103697
7. Kim H, Choe W, Lim Y, et al. Magnetic field configurations on thruster performance in accordance with ion beam characteristics in cylindrical Hall thruster plasmas. Applied Physics Letters. 2017; 110(11): 114101. doi: 10.1063/1.4978532
8. Takahashi K, Watanabe H, Nakahama Y, et al. Hall thruster ion acceleration neutralized by a radiofrequency inductively coupled plasma. Journal of Electric Propulsion. 2024; 3(1): 18. doi: 10.1007/s44205-024-00081-2
9. Linnell JA, Gallimore AD. Internal plasma potential measurements of a Hall thruster using plasma lens focusing. Physics of Plasmas. 2006; 13(10): 103504. doi: 10.1063/1.2358331
10. Reza M, Faraji F, Knoll A. Effects of magnetic field gradient and secondary electron emission on instabilities and transport in an ExB plasma configuration. arXiv preprint. 2022. doi: 10.48550/ARXIV.2212.04860
11. Andreussi T, Giannetti V, Leporini A, et al. Influence of the magnetic field configuration on the plasma flow in Hall thrusters. Plasma Physics and Controlled Fusion. 2018; 60(1): 014015. doi: 10.1088/1361-6587/aa8c4d
12. Kang X, Hang G, Zhu Z. Development and application of Hall electric propulsion technology. Journal of Rocket Propulsion. 2017; 43(1): 8. doi: 10.3969/j.issn.1672-9374.2017.01.002 (in Chinese)
13. Kim VP. Design features and operating procedures in advanced Morozov's stationary plasma thrusters. Technical Physics. 2015; 60(3): 362–375. doi: 10.1134/S1063784215030135
14. Morozov AI. The conceptual development of stationary plasma thrusters. Plasma Physics Reports. 2003; 29(3): 235–250. doi: 10.1134/1.1561119
15. Martins AA, Rodrigo M, Ferreira JL. Magnetic Field Design for a Strongly Improved PHALL Thruster. Journal of Physics: Conference Series. 2017; 911: 012024. doi: 10.1088/1742-6596/911/1/012024

16. Yu D, Zhong C, Liu X, et al. Study on a hybrid-produced magnetic-field Hall thruster. Acta Astronautica. 2024; 220: 297–304. doi: 10.1016/j.actaastro.2024.04.035
17. Deng L, Lan H, Liu Y. Numerical study on Hall thruster magnetic configuration and its optimization. Acta Physica Sinica. 2011; 60(2): 025213. doi: 10.7498/aps.60.025213 (in Chinese)
18. Peterson PY, Haas JM, Gallimore AD. Experimental investigation of Hall thruster magnetic field topography. In: Proceedings of the 27th IEEE International Conference on Plasma Science (Cat. No.00CH37087); 4–7 June 2000; New Orleans, LA, USA. doi: 10.1109/PLASMA.2000.854980
19. Ma D, Yu Q, Liu X, et al. Magnetic focusing of low-power Hall thruster with a center-mounted hollow cathode. Vacuum. 2023; 218: 112650. doi: 10.1016/j.vacuum.2023.112650
20. Fan H, Xu Y, Wang L, et al. Effects of unsymmetrical magnetic field on discharge characteristics of Hall thruster with large height-radius ratio. Vacuum. 2022; 203: 111261. doi: 10.1016/j.vacuum.2022.111261
21. Fan H, Li H, Ding Y, et al. Effects of the peak magnetic field position on Hall thruster discharge characteristics. Advances in Space Research. 2020; 66(8): 2024–2034. doi: 10.1016/j.asr.2020.06.036
22. Bombarde DS, Silla LN, Gautam SS, et al. A Comprehensive Comparative Review of Various Advanced Finite Elements to Alleviate Shear, Membrane and Volumetric Locking. Archives of Computational Methods in Engineering. 2024; 31(4): 1979–2013. doi: 10.1007/s11831-023-10050-x
23. Xu Z, Tian L, Wang P, et al. Simulation study on the influence of magnetic screen size on Hall thruster performance. Chinese Space Science and Technology. 2023; 43(4): 43–51. doi: 10.16708/j.cnki.1000-758X.2023.0052 (in Chinese)
24. Gao Y, Wang W, Li P, et al. Study on the plasma plume structures in a cylindrical Hall thruster. Vacuum. 2024; 219: 112703. doi: 10.1016/j.vacuum.2023.112703
25. Liu Q, Li Y, Hu Y, et al. Effects of Magnetic Field Gradient on the Performance of a Magnetically Shielded Hall Thruster. Aerospace. 2023; 10(11): 942. doi: 10.3390/aerospace10110942
26. Yang L, Wang PY, Wang T. Study on the influence of magnetic field on the performance of a 5 kW hall thruster. Frontiers in Materials. 2023; 10: 1150802. doi: 10.3389/fmats.2023.1150802
27. Li N, Liu Y, Liu C, et al. An integrated fluid simulation platform on Hall thruster plasmas. AIP Advances. 2022; 12(1): 015117. doi: 10.1063/5.0078222
28. Li N, Liu Y, Liu C, et al. Fluid simulation on effect of background magnetic field on plasma characteristics in a Hall thruster. AIP Advances. 2022; 12(7): 075114. doi: 10.1063/5.0096156
29. Xu Y, Kang X, Yu S. Development and Prospect of Magnetically Shielded Hall Thruster. Journal of Deep Space Exploration. 2018; 5(4): 354–360. doi: 10.15982/j.issn.2095-7777.2018.04.005 (in Chinese)
30. Vincent B, Tsikata S, Mazouffre S. Incoherent Thomson scattering measurements of electron properties in a conventional and magnetically-shielded Hall thruster. Plasma Sources Science and Technology. 2020; 29(3): 035015. doi: 10.1088/1361-6595/ab6c42
31. Voronovskyi DK, Yurkov BV, Asmolovskyi SY, et al. Improvement Lifetime of the Hall Thruster through Magnetic System Optimization. System design and analysis of aerospace technique characteristics. 2023; 33(2): 48–60. doi: 10.15421/472311
32. Liu X, Li H, Che X, et al. Optimizing a Hall thruster with aft-loaded magnetic field by aft-loading design of gas flow. Vacuum. 2024; 222: 112987. doi: 10.1016/j.vacuum.2024.112987
33. Lopedote E, Panelli M, Battista F. Scaling of Magnetic Circuit for Magnetically Shielded Hall Effect Thrusters. Aerotecnica Missili & Spazio. 2023; 102(2): 109–125. doi: 10.1007/s42496-023-00152-x
34. Rossi A, Messine F, Henaux C. A parametric optimization code based on local algorithms to design magnetic circuits of Hall effect thrusters. International Journal of Applied Electromagnetics and Mechanics. 2017; 53(2_suppl): S153–S165. doi: 10.3233/JAE-140158
35. Yu D, Liu H, Cao Y, et al. The Effect of Magnetic Mirror on Near Wall Conductivity in Hall Thrusters. Contributions to Plasma Physics. 2008; 48(8): 543–554. doi: 10.1002/ctpp.200810087
36. Wang Z, Li H, Hu Y, et al. Expanding the design freedom of the chamfered wall shape of a magnetically shielded Hall thruster. Vacuum. 2023; 207: 111603. doi: 10.1016/j.vacuum.2022.111603
37. Perales-Díaz J, Domínguez-Vázquez A, Fajardo P, et al. Hybrid plasma simulations of a magnetically shielded Hall thruster. Journal of Applied Physics. 2022; 131(10): 103302. doi: 10.1063/5.0065220
38. Zeng D, Li H, Liu J, et al. Optimization of a Long-Lifetime Hall Thruster with an Internally Mounted Cathode. AIAA Journal. 2023; 61(10): 4259–4266. doi: 10.2514/1.J062246
39. Yeo SH, Gadisa D, Ogawa H, et al. Multi-objective design optimization and physics-based sensitivity analysis of

field emission electric propulsion for CubeSat platforms. Aerospace Science and Technology. 2024; 154: 109516. doi: 10.1016/j.ast.2024.109516

40. Yeo SH, Ogawa H. Multi-Objective Design Optimization of Cusped Field Thruster via Surrogate-Assisted Evolutionary Algorithms. Journal of Propulsion and Power. 2022; 38(6): 973–988. doi: 10.2514/1.B38854
41. Slanovc F, Ortner M, Wautischer G, et al. Strategies for Global Topology Optimization for Given Stray Field Distributions. IEEE Transactions on Magnetics. 2025; 61(5): 1–15. doi: 10.1109/TMAG.2025.3554430